Journal of Power Sources, 48 (1994) 195–215

Effects of grid alloy on the properties of positive-plate corrosion layers in lead/acid batteries. Implications for premature capacity loss under repetitive deep-discharge cycling service

A.F. Hollenkamp*, K.K. Constanti, M.J. Koop and L. Apăteanu**
CSIRO Division of Mineral Products, Port Melbourne, Vic. 3207 (Australia)

M. Calábek
Department of Electrotechnology, Technical University, 662 09 Brno (Czech Republic)

K. Micka
J. Heyrovský Institute of Physical Chemistry and Electrochemistry, 182 23 Prague 8 (Czech Republic)

Abstract

Premature capacity loss (PCL) has been demonstrated consistently by the deep-discharge cycling of three-plate lead/acid cells configured with an excess of electrolyte. A capacity loss of ~2% per cycle was observed with cells based on tin-free, lead–calcium positive grids, under both constant-current and constant-voltage charging. The current that flows during constant-voltage charging decreases markedly within the first few cycles. This coincides with the establishment of an appreciable corrosion layer on the grid, and also with the onset of severe capacity loss. Significantly, there is no corresponding build-up of lead sulfate within the porous mass. With constant-current charging, a change in the overcharge factor, from 1.1 to 1.2, approximately doubles the rate of capacity loss. The corrosion products in lead–calcium plates exhibit a bi-layered structure: an outer corrosion layer of PbO_2 and an inner layer in which the composition approaches PbO. These materials are prone to fracture and separation, especially between the two layers. Cells based on lead–antimony positive grids also suffer PCL, but the rate of capacity loss (~1% per cycle) is less than that observed for the lead–calcium analogues. The current under constant-voltage charging of lead–antimony cells also decreases during the first few charge/discharge cycles, yet, this effect is over-shadowed by an increase in current due to the effects of antimony migration. Increasing the level of overcharge under constant-current charging produces only a slight reduction in cycle life. In regions close to the grid, PbO-like material is much less abundant than in lead–calcium plates. The corrosion products are composed mainly of PbO_2, and are more coherent under stress. Resistance at the grid/porous material interface, measured *in situ*, increases greatly during discharge for plates based on lead–calcium grids, but much less for the corresponding lead–antimony plates. This tends to emphasize the importance of the barrier-layer model of capacity loss, which is supported further by the observation of low-oxidation-state lead compounds in lead–calcium samples, but not in lead–antimony samples. The barrier-layer model cannot, however, provide a complete explanation for PCL: the corrosion layers of lead–antimony plates remain apparently

*Author to whom correspondence should be addressed.
**On leave from the Chemical and Biochemical Energetics Institute of Bucharest, Bucharest, Romania.

SSDI 0378-7753(93)01866-G

conductive and coherent throughout cycle life, yet, these plates suffer appreciable capacity loss. At least part of the decrease in plate performance may, therefore be due to changes in the conductivity/integrity/activity of the bulk porous mass.

Introduction

Premature capacity loss (PCL) is the name that is given to the process (or processes) that causes the discharge capacity of lead/acid cells to decline, early in service life. The phenomenon is specific to the positive plate. Examination of plates that have undergone PCL reveals little chemical or physical evidence of the degradation that has occurred [1]. It is not surprising, therefore, that many years of research have been unable to provide a full explanation of the underlying mechanism(s). PCL represents the largest single obstacle to the implementation of lead/acid batteries in several emerging energy-storage applications. The most significant of these applications is the propulsion of electric vehicles (EVs). The market for EV batteries is set to expand greatly in the next few years as a result of legislation in California that will force the introduction of so-called 'zero-emission vehicles'. The Advanced Lead-Acid Battery Consortium (ALABC), formed in 1992 under the management of the International Lead Zinc Research Organization (ILZRO), is coordinating a structured programme of research aimed at first characterizing, then overcoming, the problem of PCL. CSIRO is contributing to this programme (ILZRO Project LE-371, ALABC Project AMC 003) and the work presented here summarizes the results of recent studies.

A major aim of the work programme at CSIRO has been to clarify the importance of the various theories that have been advanced in explanation of PCL. Undoubtedly, the most widely documented of these theories is the so-called 'barrier-layer' model [1]. This model is based on the notion that capacity loss, due to the progressive isolation of positive-plate material from the grid, is caused by the development of electrical barriers in the interfacial region between the grid and the porous material (i.e., the corrosion layer). The origin of these electrical barriers is either the deposition of an insulating compound (or compounds) in the corrosion layer [2–6], or the development of fractures, concentric with the grid-wire circumference, that establishes a void between the current generator and the current collector [7].

Although many studies have reported the presence of non-conducting lead compounds in the corrosion layers of plates that have suffered PCL, few have considered the influence of the key parameters of plate design and operation on the failure mode. Factors such as the composition of the positive grid alloy, charging regime, overcharge factor, etc., all exert well-documented effects on battery performance [8]. The same parameters are also known to influence the expression of PCL. Unfortunately, the literature in this area is complicated and the information available is generally incomplete and often contradictory. We have attempted to remove some of the resultant confusion by conducting a detailed study in which the most important variables of plate performance are varied systematically under a uniform experimental regime. The results presented here focus mainly on the morphology and composition of materials in the corrosion layer. This approach has been taken, not because of any intention to exclude particular explanations of capacity loss, but rather, to deal with an issue that has, till now, received only a fragmented treatment.

Experimental programme

Table 1 provides a summary of the composition of the materials that were employed in the production of the positive plates. Table 2 outlines the key plate-processing conditions. A full description of the procedures utilized for plate production and cell assembly is available elsewhere [9]. The positive-plate grids were of a light motive-power type that measured 121 mm (height) × 142 mm (width) × 3.2 mm (thickness). They were book-mould castings, produced by East Penn Manufacturing Co. (Lyon Station, PA, USA). The alloy compositions investigated were: Pb–5.7wt.%Sb–0.3wt.%Sn ('Pb–Sb') and Pb–0.09wt.%Ca ('Pb–Ca'). Negative plates (of similar dimensions) were obtained in the cured state, also from East Penn Manufacturing Co. These plates were based on a Pb–0.09wt.%Ca–(trace Sn) grid alloy and were used as received.

Each cell consisted of one positive plate, enveloped by a glass-mat-lined polyethylene separator, and two negative plates. When completely assembled, each cell contained a substantial excess of 1.27 sp. gr. sulfuric acid solution (~6 ml per gram of positive material). Discharge was conducted at 2.5 A, to an end-of-discharge voltage of 1.75 V (= 100% depth-of-discharge (DOD)). Typical discharge times at the start of service were close to 8 h. The monitoring of plate potentials against a standard reference electrode showed that the extent of discharge was limited by the amount of positive-plate material present. This was supported by calculations of the percentage utilization of the cell-active materials. Charging was conducted by two different procedures. Both commenced at a constant current of 2.5 A, which was maintained until the cell-terminal voltage reached 2.55 V. At that point, either the terminal voltage

TABLE 1

Compositional data[a] for positive-plate materials

Plate constituent	Composition
Grid	Pb–Ca: Pb–0.09wt.%Ca Pb–Sb: Pb–5.7wt.%Sb–0.3wt.%Sn
Leady oxide	28 wt.% Pb; 62 wt.% α-PbO; 10 wt.% β-PbO
Cured material	50 wt.% α-PbO; 5 wt.% β-PbO; 44 wt.% $3PbO \cdot PbSO_4 \cdot H_2O$; 1 wt.% $2PbCO_3 \cdot Pb(OH)_2$
Formed material	9 wt.% α-PbO_2; 86 wt.% β-PbO_2; 5 wt.% $PbSO_4$

[a]Figures given are averages of several determinations.

TABLE 2

Plate-processing methods

Production stage	Process conditions
Paste production (target: 4.1 g cm^{-3})	1400 g leady oxide, 128 ml sulfuric acid (1.40 sp. gr.), 210 ml water, 1.1 g fibre, 1.4 g CMC[a]
Plate curing	50 °C and 100% r.h. for 24 h; drying for 4 h
Plate formation	72 h at 1.8 A per plate, including 2×4-h rest period, 40 °C

[a]CMC = carboxymethyl cellulose.

was held constant at 2.55 V (constant-current–constant-voltage charging, CC–CV) or the current was held constant, at a lower value of 1.0 A (two-step constant-current, two-step CC). In both methods, charging was stopped once the overcharge factor (= ratio of input charge to charge removed in previous discharge, or C/D) reached a predetermined value. In this study, C/D values of 1.1 and 1.2 were utilized. The charge/discharge service of cells was terminated, except in special cases, once the capacity had fallen to approximately 50% of the initial value.

X-ray diffraction (XRD) analysis of the phase composition of positive-plate material was based on the output from a Philips (Eindhoven, The Netherlands) Model PW1710 diffractometer fitted with a Cu Kα X-ray source. Samples were prepared as finely ground powders. Analysis for sulfur (as lead sulfate) in negative-plate material was conducted with a LECO (Michigan, USA) Model CS-244 carbon and sulfur induction furnace. Sulfur was detected with an infrared detector, as sulfur dioxide. Electron probe microanalysis (EPMA) was performed on a CAMECA (Paris, France) Camebax 'Microbeam' instrument that was operated at an accelerating voltage of 15 kV and a beam current of 60 nA. The elements analysed, along with the respective analytical spectral lines, were: lead (Mα), sulfur (Kα), and oxygen (Kα). Raw intensity ratios were corrected for matrix effects by means of the 'PAP' matrix corrections [10]. A calibration analysis for lead and oxygen was carried out on a sample of plattnerite (PbO_2), while sulfur analysis was standardized with data for a sample of pyrite. Prior to analysis, both standard and unknown were coated simultaneously with a thin (~20 nm) film of carbon. Data were acquired and processed under software control by means of PC–MICROBEAM™ version 1.0 [11].

Scanning electron microscopy (SEM) was carried out with a JEOL (Tokyo, Japan) Model JSM-25S III microscope that was operated at an accelerating voltage of up to 25 kV. Samples were taken from positive plates in a two-step process. First, small portions of washed and dried plate material were removed by careful excision. As illustrated in Fig. 1(a), each portion consists of a grid wire and a 'pellet' of positive material. The latter was broken away from the adjacent grid wire and the exposed surfaces (grid and pellet) were examined by SEM, Fig. 1(b). Typically, cleavage occurred very close to the grid wire. A thin coating of carbon was applied to each sample. The

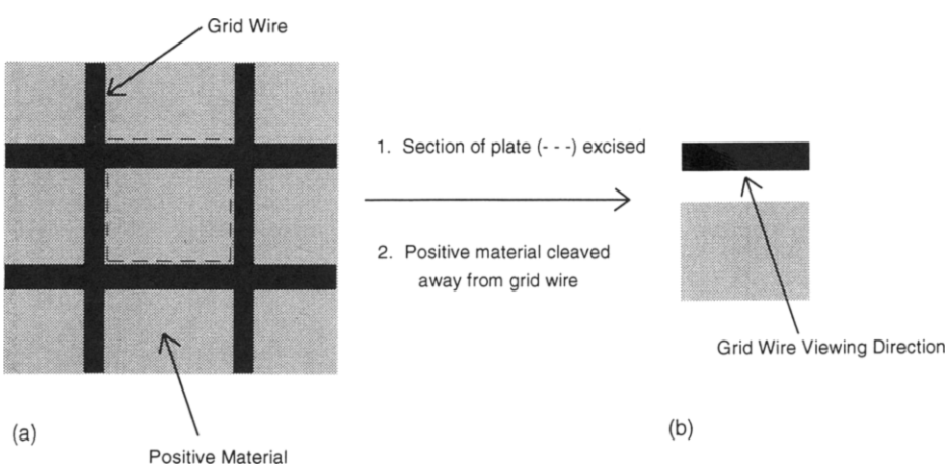

Fig. 1. Preparation of samples for scanning electron microscopy: (a) portion excised from plate; (b) pellet and grid wire separated for examination.

second stage of sample preparation for microscopy involved the mounting of the remainder of the positive plate in epoxy resin. After setting, sections ($\sim$1 cm^2) were then cut out and polished by abrasion with successively finer grades of carborundum paper. Final polishing was carried out by lapping with diamond paste of 6, 3 and, finally, 1 μm. A thin coating of carbon was applied prior to imaging.

Measurements of the electrical resistance in the region between the grid and the active (porous) material were conducted *in situ* by a method that has been utilized in several extensive studies of resistance in lead/acid battery plates [12–14]. Full details of the technique are described elsewhere [14]. The technique requires the construction of a parallel arrangement of lead/lead-alloy wires (the grid) that serves as the basis for a pasted plate. In the absence of any cross connection between wires, the resistance is measured when current is passed across the plate (i.e., from the outermost wire on one side to the outermost on the other side of the plate). A straightforward mathematical analysis yields values for the resistance of both the porous material (between the wires) and the material between the grid and the porous mass. For the present study, vertical grid wires were cut from several Pb–Sb and Pb–Ca grids (taken from the supply used for manufacture of plates in the cycling study). To provide comparative data, measurements were also conducted on several other grid alloys. The grid wires were arranged and set in the geometry required for the measurement of resistance. Further treatment followed the established procedures [14]. After preparation, each positive plate was incorporated into a cell with two negative electrodes. The cell configuration also featured an excess of electrolyte. Prior to the first measurement, each cell was subjected to 5 charge/discharge cycles. It should be noted that the paste utilized in the preparation of test plates was not the same as that produced for the plates in the cycling study. For this reason, no attempt has been made to compare the composition and/or structure of materials from the two series of experiments.

Results

Effect of charge regime on cycle life

A summary of the performance of cells cycled under CC–CV charging is shown in Fig. 2. The plot for Pb–Sb, which is an average for 11 cells, indicates that capacity was constant for approximately the first 10 cycles after which a gradual decline occurred. By comparison, Pb–Ca cells (average plot for 16 cells) lost capacity immediately and at a substantial rate, especially during the first 10 cycles. Another aspect of the performance of Pb–Ca cells is that they exhibited very low charging current once the constant-voltage phase had begun. This behaviour was never present in newly formed cells, but developed during the first 10 cycles. In many cases, the current fell to close to the detection limit of the charge-control equipment. This behaviour extended greatly the length of time required for complete charging (i.e., for reaching the specified overcharge factor). The Pb–Sb cells displayed only small increases in constant-voltage charging time and, thus, completed each charge/discharge cycle in much less time. Subsequent investigation indicated that the primary cause of the difference in constant-voltage charging behaviour was the influence of the depolarizing effects of antimony. Evidence suggested that, in the Pb–Sb cells, the reduction in the overpotential for evolution of hydrogen at the negative plate (due to migration of antimony from the positive plate) allowed substantial charging current to flow. In the Pb–Ca cells, both positive and negative plates were antimony-free so that no enhancement of hydrogen

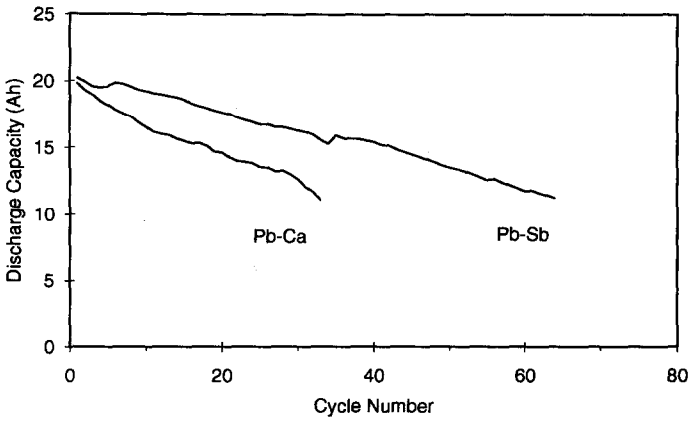

Fig. 2. Discharge performance of cells subjected to CC–CV charging.

evolution was possible. Therefore, charging current remained low for Pb–Ca cells. This reasoning explains the difference in charging behaviour once the cells had completed several cycles. It may not, however, account for the decrease in constant-voltage charging current that occurred during the first 5 to 10 cycles. That phenomenon is more likely to be consistent with a process such as the growth and development of the grid corrosion layer.

Concern that the large difference in charging time might influence the demonstration of PCL prompted the development of a procedure without a constant-voltage phase; the result was the two-step CC method. Surprisingly, the performance of cells charged by the two-step CC method was virtually indistinguishable from that shown in Fig. 2 for CC–CV charging. Pb–Ca cells (13 examples) suffered a more severe loss of capacity than their Pb–Sb analogues (8 examples): the difference in the rate of capacity loss was close to a factor of two. Capacity-loss profiles for each type of cell were, therefore, largely unaffected by the choice of charging method. Later examination of samples from failed cells showed that both the phase composition and the morphology of positive materials were also not influenced by a change in the charging procedure. In later discussions of failure modes, therefore, no distinction is made between samples derived from plates charged by different methods.

Under two-step CC charging, an increase in the overcharge factor (C/D), from 1.1 to 1.2, caused a distinct reduction in the cycle life of Pb–Ca cells. Figure 3 provides a comparison of the averaged profiles for discharge capacity against time (C/D = 1.1 and 1.2). Pb–Ca cells charged at C/D = 1.2 suffered a loss of capacity at approximately twice the rate of those charged at C/D = 1.1. The capacity loss of the former cells did, however, abate once the capacity had fallen to ~50% of the initial value. There was no obvious reason for this behaviour. For Pb–Sb cells, the difference in rate of capacity loss under the two overcharge factors was not as marked. Capacity loss was ~30% higher with the greater overcharge (C/D = 1.2). This difference in performance is of the same order as the statistical spread of data for all Pb–Sb cells. For Pb–Ca cells, however, the separation of behaviour was much greater.

Phase composition of failed plates

Before analysing the materials from each failed cell, a postmortem examination was conducted to determine the principal cause of failure. Visual inspection revealed

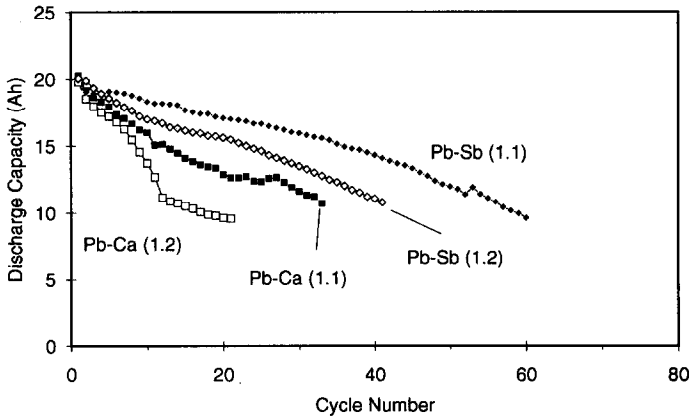

Fig. 3. Comparative discharge performance of cells at different levels of overcharge under two-step CC charging. Figure in parentheses is the actual overcharge factor.

TABLE 3

Phase composition (wt.%) of charged positive-plate material from both Pb–Ca and Pb–Sb cells

Stage of service	β-PbO_2	α-PbO_2	$PbSO_4$
Formed[a]	84–87	8–10	3–6
Cycled[b]	96–99	<1–3	0–2

[a]Initial (100%) capacity.
[b]Capacity=50% of initial value.

some buckling (warping) of the plates. Plates with Pb–Ca grids displayed a greater degree of buckling than those with Pb–Sb grids. The extent of the distortion was, however, variable and, importantly, there was no correlation with the rate of capacity loss. The loss of positive material ('shedding') was also assessed for failed plates. More material was shed from Pb–Sb than from Pb–Ca cells. On average, the antimonial cells lost 25% of the total porous mass during cycling, while Pb–Ca cells lost 10%. This difference in the amount of shed material was related mainly to the difference in the cycle lives for the two types of cells (Fig. 2). As anticipated, the common physical modes of degradation could not be removed entirely, and their influence on plate performance increased with the number of cycles completed.

Prior to carrying out XRD phase analysis, samples of positive-plate material were removed from the plate, washed with water until they were largely free of sulfuric acid, then dried for several hours at 105 °C. It was found that the phase composition was remarkably consistent throughout the entire range of cycled cells and showed no variation with grid-alloy composition. The data, expressed as a range of values for each phase, are summarized in Table 3. Comparison of these data with those recorded after formation (also provided in Table 3) shows that the abundance of α-PbO_2 decreased during cycling, as expected. In addition, cycled material contained remarkably low levels of lead sulfate. Chemical analysis of selected samples was conducted in order to determine the total abundance of lead sulfate in the material. (Note, XRD methods are only able to quantify crystalline material above a minimum crystallite

size.) The results showed that XRD underestimated the abundance of lead sulfate by approximately 2 wt.%. Thus, cycled positive material contained a small amount of lead sulfate that was either amorphous or comprised of very small crystallites.

The study of the phase composition of positive-plate materials was expanded to include samples taken from plates in the discharged state. For each alloy, five cells that had failed were sampled in both the charged and discharged (100% DOD) states. On the final discharge before removal from service, all of the plates yielded similar values of capacity. The samples of material were subjected to both XRD phase analysis and chemical analysis for sulfur (as lead sulfate). The results, expressed as averages for each type of positive plate, are summarized in Table 4. As expected, the phase composition in the discharged state, for both types of plate, showed significant amounts of lead sulfate. Yet, a greater proportion of lead dioxide was converted to lead sulfate in the antimonial cells, compared with the calcium analogues. Although the difference is small on the basis of XRD data, it is more pronounced according to the results of chemical analysis. (The latter findings must be given greater weighting because they reflect all of the material sampled; the XRD data only provide information on the crystalline fraction of the material.) The fact that the fractional utilization of positive material was greater in Pb–Sb plates than in Pb–Ca analogues has an important corollary: Pb–Ca based plates possessed more of what was essentially 'inactive' lead dioxide at the end of service. In other words, Pb–Ca plates that yielded the same capacity at failure as the Pb–Sb plates, did so through the discharge of a smaller proportion of the plate material present.

Structure of corrosion layers

Earlier work in our laboratories [15–17] surveyed the composition and morphology of positive-plate material at various stages of service, under the adopted experimental regime. As a general conclusion, material in the bulk of the positive mass, far from the grid, was found to be similar, both chemically and structurally, in samples from cells based on Pb–Ca and Pb–Sb grids. By contrast, later work provided some indication of differences in the morphology of material close to the grid [9]. In particular, the choice of grid alloy was found to exert a marked effect over the physical properties of the compounds formed in and around the corrosion layer during cycling. As this finding lies close to the concepts behind one of the main theories of PCL (viz., the barrier-layer model, *v.s.*), a detailed investigation of corrosion-layer characteristics was instigated.

TABLE 4

Phase composition (wt.%) for positive-plate material from failed cells[a]

State of charge	Grid alloy	β-PbO_2	α-PbO_2	$PbSO_4$	$PbSO_4$[b]
Charged	Pb–Sb	97	1	2	4
	Pb–Ca	98	<1	2	4
Discharged[c]	Pb–Sb	66	<1	33	46
	Pb–Ca	72	<1	27	30

[a]50% of initial capacity.
[b]Determined by chemical analysis.
[c]100% DOD.

In order to establish a baseline for comparison of cycled materials based on the two grid alloys, we began by examining samples from the two types of plate before the commencement of cycling. Figure 4 provides a typical view of material in the corrosion layer of a plate with a Pb–Ca grid that was removed in the formed state. The image is for a cleaved, or 'rough' sample that was prepared by breaking a pellet of porous material away from the attached grid wire (see Fig. 1 for details). This image focuses on the grid-based portion. The micrograph is characterized by large particles that are rectilinear in outline, but have concave, 'hollowed out' faces. This material is almost certainly crystalline lead sulfate that has not been converted completely to lead dioxide during plate formation. Similar images were obtained for samples from formed Pb–Sb plates that were prepared in the same manner.

The cross-sectional view of a polished portion of a formed Pb–Ca plate (Fig. 5) shows the features that lie beneath those surface formations seen in Fig. 4. There is a prominent corrosion layer, the thickness of which varies between 5 and 10 μm. Considerable variation in composition was found within this layer. A trace of material of darker shade actually travels all the way through the layer, both parallel and close to the grid perimeter. As labelled in Fig. 5, this dark trace returns composition, by EPMA analysis, that is close to the formula $2(PbO_2)\cdot PbSO_4$. The remainder of the corrosion product is predominantly lead dioxide. Traces of darker material, similar in appearance to those within the corrosion layer, are also noted just outside (porous material side) the layer. The elemental composition of these regions suggests that they are the quasi-crystalline formations exposed in Fig. 4.

Figure 6 shows a typical cross-sectional view of a formed Pb–Sb plate. The Pb–Sb grid is encased in a thick, compact band of material. This material returns a composition close to that of lead dioxide, although appreciable levels of lead sulfate are also

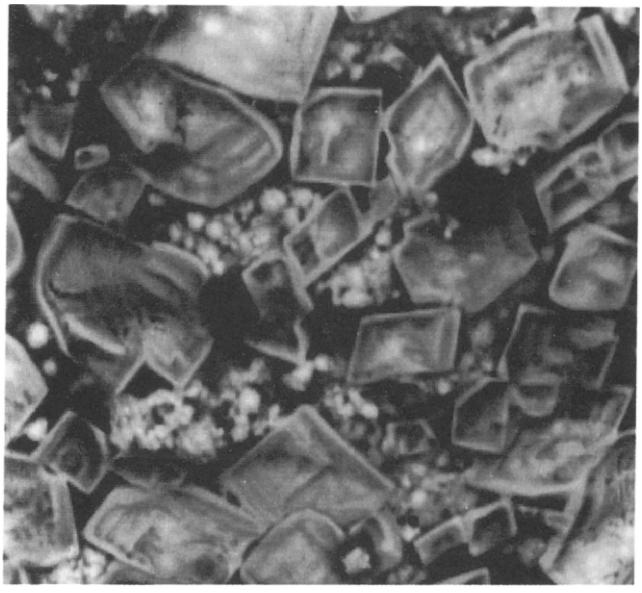

Fig. 4. Secondary-electron micrograph of the surface of a grid/corrosion layer sample from a formed Pb–Ca positive plate. Bar length: 10 μm.

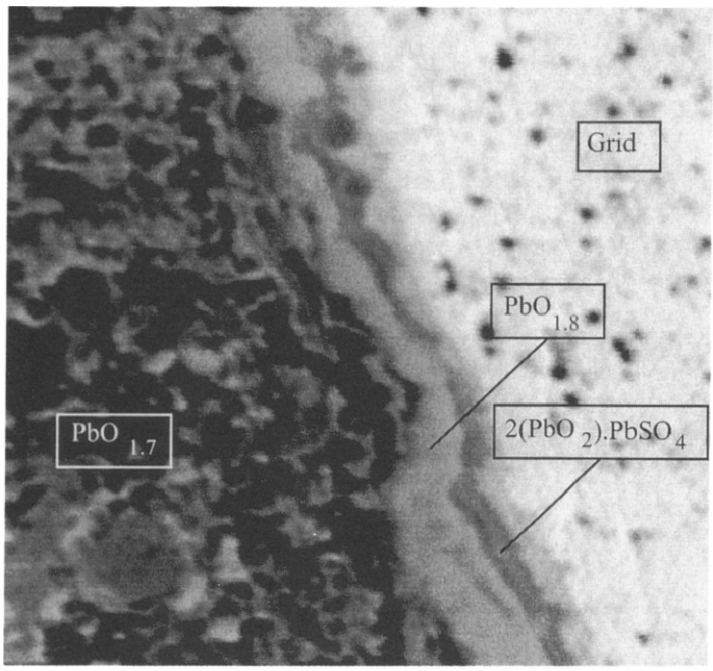

Fig. 5. Backscattered-electron micrograph of the cross section of a sample from a formed Pb–Ca positive plate. Bar length: 10 μm.

present. The data are consistent with the composition $6(PbO_2) \cdot PbSO_4$. Several regions yielded the same elemental distribution as the grid (i.e., mainly lead and antimony) and are, therefore, assigned to isolated portions of grid metal. The formation process has converted most of the outer 40 to 50 μm of grid into the so-called 'corrosion layer'. The presence of the crystalline material noted in the cleaved sample is also evident in Fig. 6. At the boundary of the porous bulk material with the dense corrosion layer, patches of relatively dark material can be seen. Elemental analysis showed that the darker regions were much richer in lead sulfate than the surrounding material (analysis gave $PbO_2 \cdot PbSO_4$). These regions are assigned to partially formed deposits of lead sulfate.

By comparison with the Pb–Ca sample, a much larger amount of the Pb–Sb grid was attacked during formation. This is most likely due to the large differences in the structure and the chemical composition of the two alloys. The similarity between cleaved samples based on the two alloys clearly only applies to the exposed surface of those samples. Cross-sectional viewing indicates that there are major differences in the corrosion-layer materials, in terms of both the extent of corrosion during formation and the composition of the products of corrosion. Therefore, a clear distinction between the two types of positive plate is apparent, before charge/discharge service commences. It may also be significant that the residual lead sulfate in the formed state lies external to the dense corrosion layer for Pb–Sb, but is bound well within the corrosion layer for Pb–Ca.

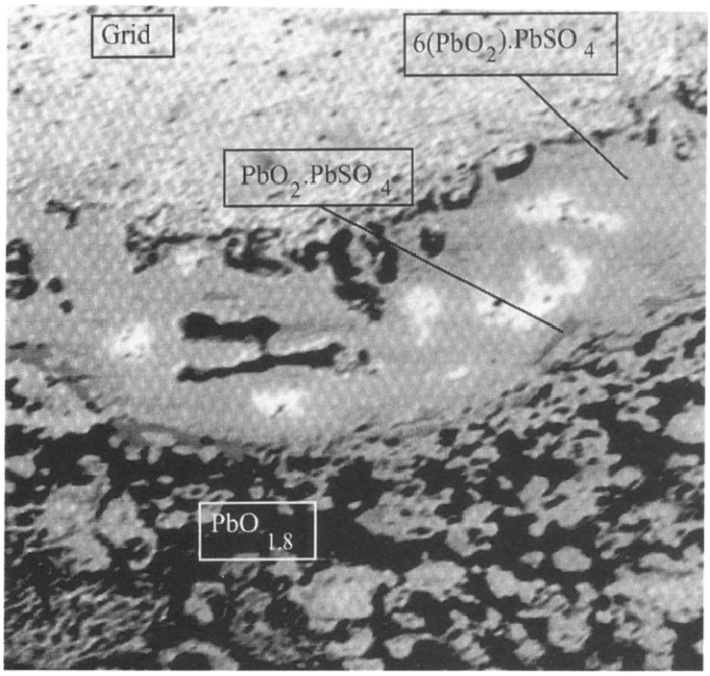

Fig. 6. Backscattered-electron micrograph of the cross section of a sample from a formed Pb–Sb positive plate. Bar length: 50 μm.

At the completion of service (discharge capacity at 50% of initial value), it was found that substantial changes had occurred in the positive material near the grid, for both grid alloys. Figure 7 shows a secondary electron micrograph of the region near the grid in a failed Pb–Ca positive plate (removed in the fully charged state). This image is remarkable for the way in which it reveals the three major components of the positive plate (labelled in Fig. 7). As described earlier, the procedure for preparing cleaved samples is designed to expose the material in the regions where the coherence of the material is least. The clear impression from such images is that the corrosion products in plates with Pb–Ca grids exhibit a clearly defined, layered structure. Under applied stress, the constituent layers are prone to separate from each other and from the underlying grid. A complementary view of the corrosion-layer structure is afforded by preparing a cross-sectioned sample from a cycled Pb–Ca plate. A typical image is shown in Fig. 8. The transition from grid (left side of image) to porous positive material (right side) passes through at least two distinct layers of densely packed deposits. Compositional data from EPMA showed that material in the bulk, away from the grid, was mostly lead dioxide, as anticipated. A composition close to lead dioxide was also obtained for the material in the dense corrosion layer that formed a ring around the grid. Underneath this layer were found zones of another corrosion product. This inner corrosion layer occurred to varying extents and compositional data ranged from $PbO_{1.2}$ to $PbO_{1.0}$. This range clearly identifies the material as consisting mainly of lead(II) oxide, an insulator in its pure form. This product ranged in abundance from discrete pockets to complete layers that totally surrounded

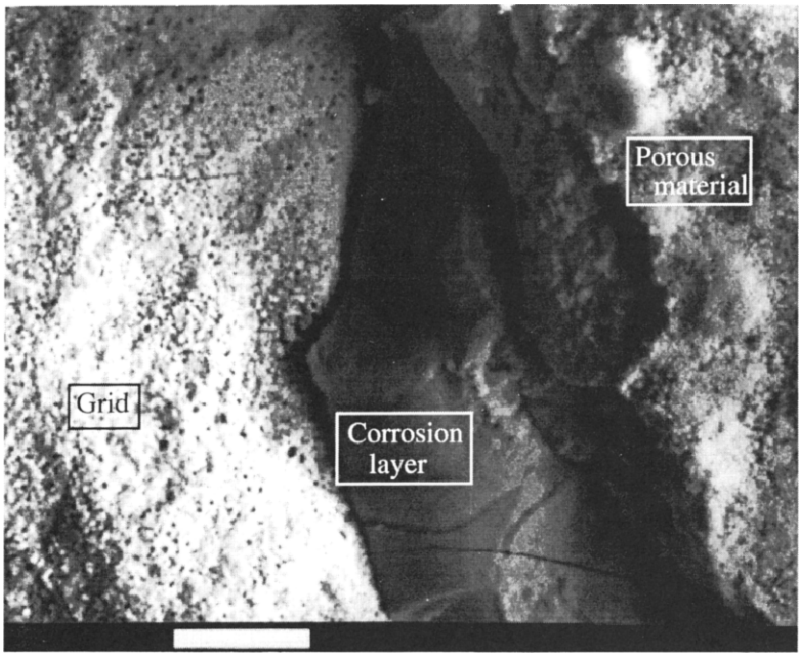

Fig. 7. Secondary-electron micrograph of a grid/corrosion layer sample from a cycled (C/D = 1.1) Pb–Ca positive plate sampled in the charged state. Bar length: 10 μm.

the grid. Physical separation of the two layers is also noted (Fig. 8) and other images also showed separation of the inner layer from the adjacent grid.

The analogous Pb–Sb samples displayed quite different morphology within the corrosion zone, as demonstrated by the cross-sectional view in Fig. 9. The main difference between this image and that for a Pb–Ca plate (Fig. 8) lies in the distinctly patterned layer of material surrounding the corrosion layer in the antimonial sample. This is referred to as the 'dendritic' layer, because of its branched appearance, and it was observed in all samples from cycled Pb–Sb plates. Excluding this dendritic layer, the corrosion-layer thickness for Pb–Sb and Pb–Ca samples was approximately constant. Pb–Sb corrosion layers did not, however, exhibit any sign of the thin bands of low-oxidation-state lead oxides that were seen in Pb–Ca samples. Rather, the material near the grid in Pb–Sb samples was composed almost entirely of lead dioxide. Several cracks are present in the corrosion layer (Fig. 9), but these are much shorter than the long, continuous fractures seen in the corresponding Pb–Ca samples (e.g., Fig. 8). When attempts were made to cleave the pellet of porous material away from the grid (Fig. 1), separation occurred preferentially either within the corrosion layer or between the corrosion layer and the dendritic layer. The corrosion products tended to adhere strongly to the grid. The bond between corrosion layer and Pb–Sb grid is clearly a relatively strong one.

It is worth noting at this point that a brief investigation was made of the number of cycles that were required for the development of the corrosion-layer structures shown in Figs. 8 and 9. This issue was of interest in relation to the rapid drop in constant-voltage charging current that occurred within the first few cycles of operation, especially for Pb–Ca cells. Accordingly, examinations were conducted on a typical Pb–Ca positive plate after three charge/discharge cycles. In this short period, the

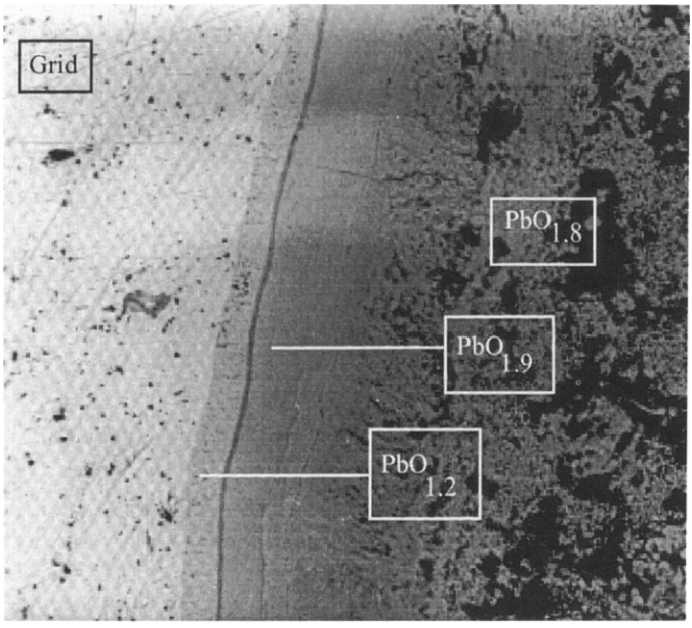

Fig. 8. Backscattered-electron micrograph of a cross section through a cycled (C/D = 1.1) Pb–Ca positive plate sampled in the charged state. Bar length: 50 μm.

charging current of the cell had fallen greatly, yet discharge capacity was almost unchanged from the initial value. Typical cross-sectional views of this plate were found to be similar to that of Fig. 8. Specifically, the thickness of the corrosion layer was within the range of values found for plates cycled to failure, and a continuous band of lead oxides (average composition $PbO_{1.2}$) was detected adjacent to the grid. Given that the corrosion layer is known to be much thinner prior to the start of charge/discharge duty (Fig. 5), it is clear that significant changes take place in this region of the positive plate during the first few cycles of operation. The coincidence of the decrease in charging current with the thickening of the corrosion layer suggests further work should be conducted on the association of these two phenomena.

Increasing the overcharge factor for the cycling of Pb–Ca cells caused a sharp decrease in cycle life (see Fig. 3). The same treatment of Pb–Sb cells resulted in a less-pronounced shortening of service life. Typical backscattered-electron micrographs of positive-plate cross sections from cells cycled at C/D = 1.2 with the two-step CC charging procedure were similar, in terms of both composition and morphology, to those obtained at C/D = 1.1. For a Pb–Sb grid, measurements of the thickness of layers within the region close to the grid showed that the corrosion zone was thicker at the higher overcharge factor. The result is, of course, consistent with expectations. The Pb–Sb cells cycled at higher overcharge yielded only slightly shorter cycle lives. Thus, the total amount of overcharge, over the life of the cells, was greater for Pb–Sb cells cycled at C/D = 1.2. For Pb–Ca samples, the choice of overcharge factor exerted no obvious effect on the structure of the corrosion layer. In both cases (C/D = 1.1 and 1.2) the corrosion region was clearly bi-layered (as in Fig. 8) and the elemental

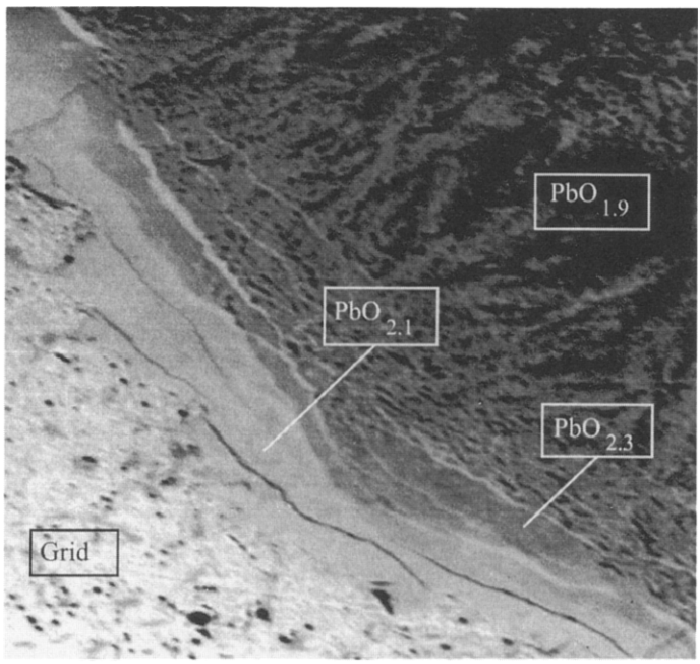

Fig. 9. Backscattered-electron micrograph of a cross section through a cycled (C/D = 1.1) Pb–Sb positive plate sampled in the charged state. Bar length: 50 μm.

composition of each corresponding layer was similar. These findings demonstrate that material in the corrosion zone of failed positive plates is similar, both dimensionally and compositionally, when cells are cycled under different overcharge factors. Whether features of the corrosion layer are related to the cause(s) of capacity loss remains unsolved.

A comparison of morphology was made between cycled positive-plate materials from both calcium and antimonial plates in the fully charged and discharged (100% DOD) states. Figure 10 shows a typical cross-sectional view of a Pb–Ca positive plate that was removed from service in the discharged state. Regions within the cross section are labelled and an assignment of the average elemental composition for each of these regions has been included. The distinct inner corrosion layer detected in the charged state (Fig. 8) was also present in the discharged state. The composition of the layer was found to be close to PbO, although there was some difference in the ratio of oxygen to lead (viz., discharged: 1.3; charged: 1.2). Due to the semi-quantitative nature of the EPMA method, this difference is of the same order as the range of compositions that is encountered within regions of nominally the same compound. For failed Pb–Sb plates in the discharged state, lead dioxide was the dominant phase in the corrosion layer, as noted in the charged state (Fig. 9). A relatively small number of samples was also characterized by an inner corrosion layer that contained lead sulfate. Determination of the composition of material in the bulk of the porous mass from both types of discharged positive plate was also carried out. As expected, the results indicated appreciable concentrations of sulfur, consistent with the discharged state of the plate

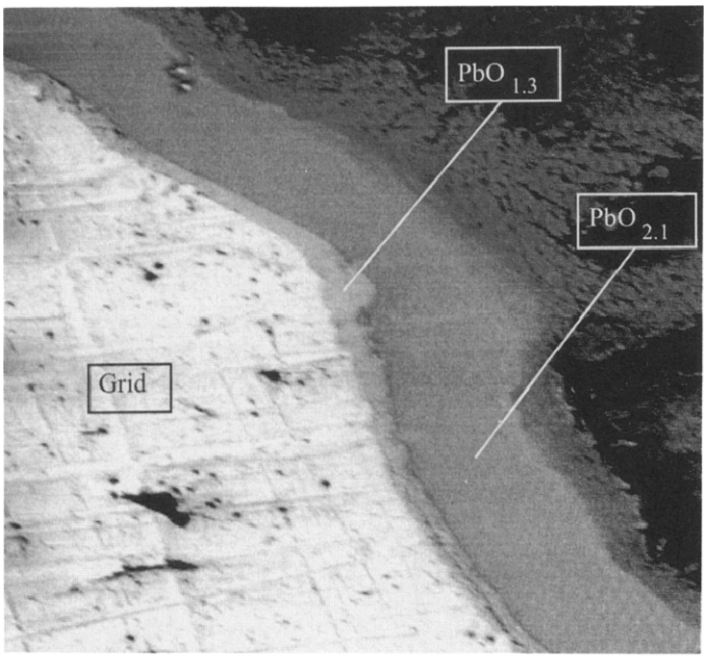

Fig. 10. Backscattered-electron micrograph of a cross section through a cycled (C/D = 1.1) Pb–Ca positive plate sampled in the discharged state. Bar length: 50 μm.

materials. The XRD data for material from the same plates (Table 4) provide a quantitative evaluation of the extent of discharge (see also earlier discussion, above).

Resistance at the grid/active-material interface

In order to investigate further the role played by corrosion-layer material in the loss of positive-plate capacity, measurements of resistance were carried out *in situ*. Experimental plates were assembled with a range of grid alloys, including the two alloys on which the above cycling studies were conducted. The composition of each alloy is as follows: no. 1 — pure Pb; no. 2 — Pb–0.1wt.%Ca; no. 3 — Pb–0.1wt.%Ca–0.2wt.%Sn; no. 4 — Pb–2.2wt.%Sb–0.1wt.%Sn; no. 5 — Pb–2.4wt.%Sb; no. 6 — Pb–5.3wt.%Sb; no. 7 — Pb–5.7wt.%Sb–0.3wt.%Sn. With respect to the cycling studies already described, alloy no. 2 is 'Pb–Ca' and alloy no. 7 is 'Pb–Sb'. The resistance between the grid and the porous material, R_k the 'contact' resistance, was measured at regular intervals during the discharging of plates based on each of the alloys. For each measurement, the plate was disconnected from the load and lifted out of the electrolyte solution. The results for discharging plates at a relatively low rate (approximate discharge time = 30 h) to 100% DOD (end-of-discharge voltage = 1.75 V) are presented in Fig. 11. The plots of R_k against DOD reveal enormous differences in the magnitude of the contact resistance during discharge. At the start of discharge, R_k values span a range of ~100 mΩ. By the end of discharge, R_k spans several thousand mΩ. The largest increases in resistance occur in the plates based on pure lead and Pb–Ca, while the Pb–Sb alloy used in the cycling studies undergoes only a relatively small

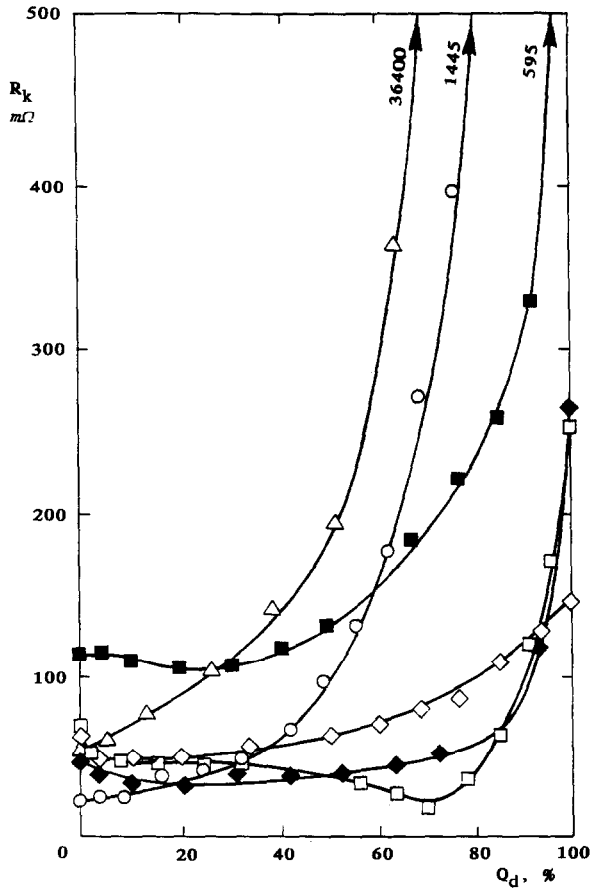

Fig. 11. Contact resistance (R_k) vs. percent discharged capacity (100% DOD) for positive plates based on the following grid alloys: (△) pure Pb; (○) Pb–0.1wt.%Ca; (◇) Pb–2.2wt.%Sb–0.1wt.%Sn; (◆) Pb–2.4wt.%Sb; (■) Pb–5.3wt.%Sb; (□) Pb–5.7wt.%Sb–0.3wt.%Sn. Discharge time ≅ 30 h.

increase. In addition, a strong effect of tin on resistance is indicated. Comparison of the two medium-antimony alloys shows that the one with tin (no. 4) exhibited an end-of-discharge resistance that was lower than that for the tin-free alloy (no. 5) by approximately a factor of two. Similarly, the corresponding difference for the high-antimony alloys (nos. 6 and 7) is also a factor of two.

Figure 12 summarizes the results of a second series of resistance measurements at a higher rate of discharge (approximate discharge time = 5 h; end-of-discharge voltage = 1.75 V). The results follow a similar trend to those shown in Fig. 11, although resistance rises more gradually with depth-of-discharge. This is because the extent of utilization of positive material is lower at the higher rate. There is also likely to be an effect related to the difference in current distribution, across the plate, at the two rates of discharge. Nevertheless, the results of Fig. 12 support the conclusions from Fig. 11 that antimonial plates exhibit smaller increases in contact resistance during discharge than either pure lead or Pb–Ca plates. Again, an effect of tin in reducing the increase in R_k is apparent. This series of results includes a comparison of a tin-

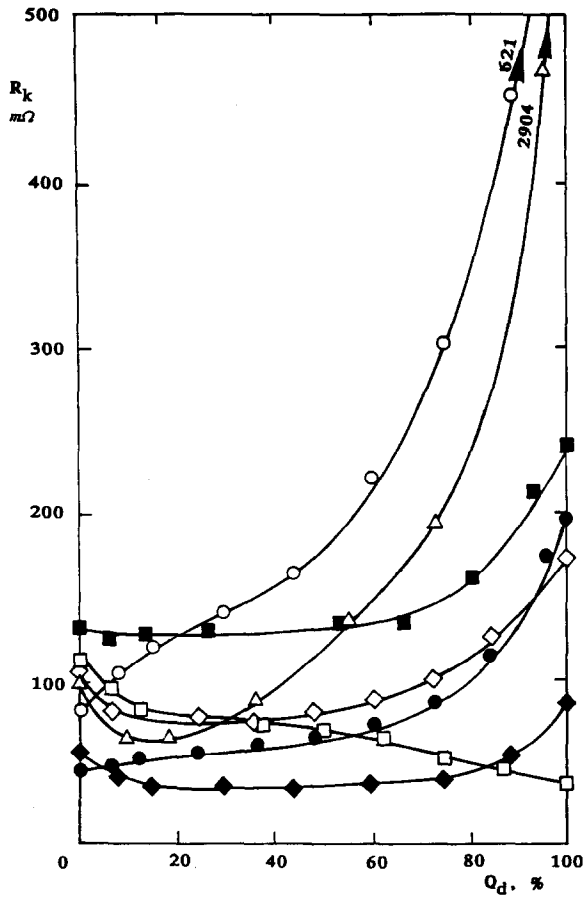

Fig. 12. Contact resistance (R_k) vs. percent discharged capacity (100% DOD) for positive plates based on the following grid alloys: (△) pure Pb; (○) Pb–0.1wt.%Ca; (●) Pb–0.1wt.%Ca–0.2wt.%Sn; (◇) Pb–2.2wt.%Sb–0.1wt.%Sn; (◆) Pb–2.4wt.%Sb; (■) Pb–5.3wt.%Sb; (□) Pb–5.7wt.%Sb–0.3wt.%Sn. Discharge time ≅ 5 h.

free Pb–Ca grid (no. 2) with a typical tin-containing Pb–Ca grid (no. 3). The plate based on the former alloy exhibits an increase in resistance that is greater than that for the latter alloy, by more than a factor of three. The role of tin under these conditions is not straightforward, though, because the order of the two medium-antimony alloys (nos. 4 and 5) is now reversed, compared with the results at the longer discharge time (Fig. 11). It is also noteworthy — indeed, even surprising — that the plot for antimonial alloy no. 7 (used in the cycling work) displays a downward trend throughout the second half of discharge.

Discussion

In the context of previous studies of PCL, the results obtained here represent a significant advancement in knowledge of the phenomenon. Several key aspects of PCL

have, until now, generated confusion, due either to a lack of information or to conflict between reported studies. Much of this complexity has now been removed. Perhaps the most crucial issue that has been resolved is the performance of cells based on high-antimony (>5 wt.% Sb) positive-plate grids, under conditions that cause PCL. It is widely believed that such cells are immune to PCL. Yet, the findings of this study show clearly that this is far from true. Rather, deep-discharge cycling has been found to cause capacity loss in both Pb–Ca and Pb–Sb cells. The difference in performance of the two types of cell is expressed specifically in the rate of capacity loss. The inclusion of antimony in the positive-plate grid reduces the severity of capacity loss, but the ultimate performance is still limited by the process(es) that constitute PCL.

Although typical Pb–Ca and Pb–Sb positive plates yield charge/discharge performance of the same order, samples of plate materials from the two systems at failure differ considerably. These differences apply to both the corrosion layer and the bulk of the porous material. The illustrations given in Fig. 13 summarize schematically the observations that have been made to date. At failure, Pb–Ca plates retain more porous material than the corresponding Pb–Sb plates, but, as a result, a smaller portion is utilized in the discharge process. Clearly, there is potentially more available capacity in the Pb–Ca plate, but it is not accessible. This non-accessibility is due to: (i) isolation of porous material from the grid (e.g., in accordance with the barrier-layer model); (ii) an intrinsic deactivation/isolation within the porous structure (e.g., as in the Kugelhaufen model [18, 19] and the gel–crystal model [20]); (iii) a combination of (i) and (ii). Clearly, we have obtained a great deal of circumstantial evidence of (i) in the demise of Pb–Ca cells. A thin inner corrosion layer that is comprised mainly of an insulating compound is present from early in cycle life through to failure. Measurements revealed large increases in resistance in the same region during the discharge process. There was, however, no obvious compositional change in this region when examinations were conducted on samples in the discharged state. This does not, of course, discount the evidence from resistance data. The changes during discharge that cause the increase in resistance may, in fact, be due to subtle alteration of electronic structure within the corrosion layer, rather than to gross chemical processes such as the conversion of lead dioxide to lead sulfate. In fact, the absence of lead sulfate in the corrosion-layer material from all of the discharged Pb–Ca samples is quite remarkable. It is certainly an observation that conflicts with some of the previous work on capacity loss [5].

By comparison, Pb–Sb cells cycle longer and, in that time, shed more material. While more of the capacity loss can, therefore, be ascribed to this process than for Pb–Ca, a large fraction must still be attributed to unknown phenomena, viz., PCL. For Pb–Sb, however, evidence of PCL, in terms of the well-known theories such as the barrier-layer model, is extremely scarce. The corrosion-layer region of each of the samples examined was dominated by compounds that were very close in elemental composition to lead dioxide. Lower oxides of lead (composition approaching PbO) were only found in small isolated zones; complete rings of such materials were never observed. Similarly, examination of corrosion layers in the discharged state revealed a preponderance of lead dioxide, although a few samples displayed layers rich in lead sulfate next to the grid. Importantly, the resistance of the (Pb–Sb)-grid/porous-material interface did not increase appreciably during discharge, although at least some of this effect may be due to the presence of tin in the alloy.

At the time of writing, the studies of plate resistance were incomplete as only the data for contact resistance were available. For a full discussion of this topic, it will be necessary to consider also the corresponding changes in the resistance of the

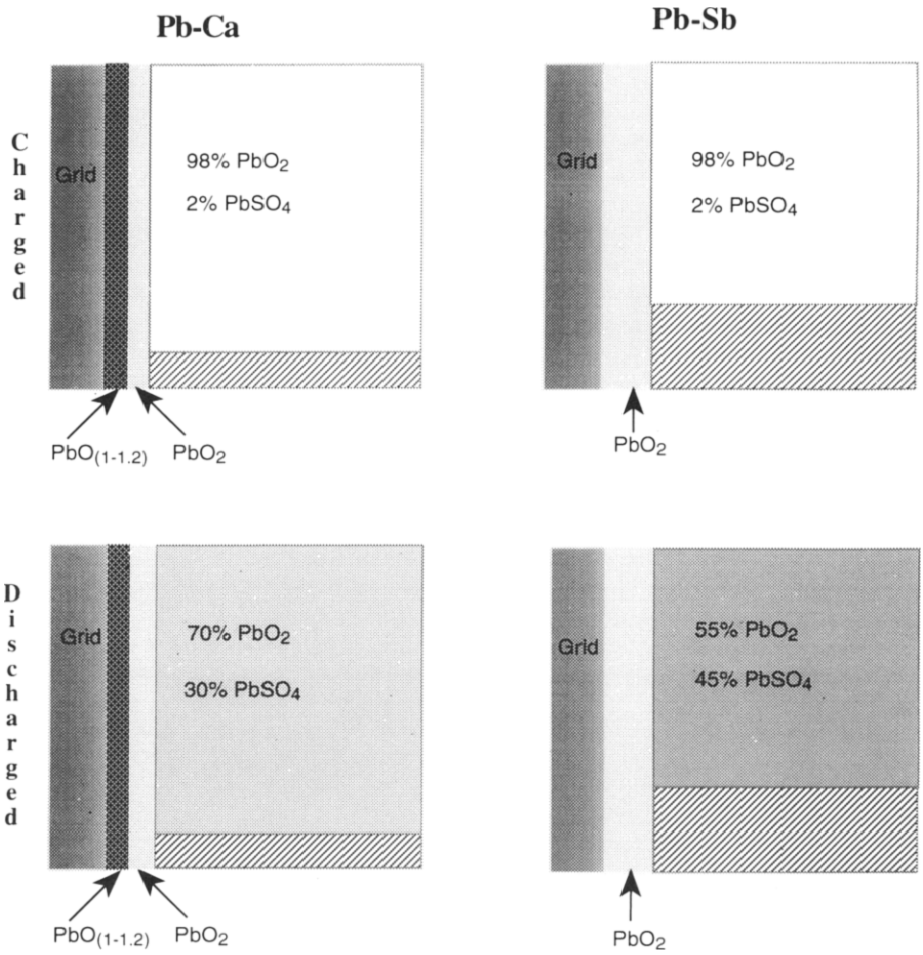

Fig. 13. Schematic summary of the condition of positive plates at failure. Hatched region represents the proportion, but not the location, of porous material that was lost from each plate through shedding.

bulk porous material. Nevertheless, it is worth noting that the results for contact resistance during discharge parallel, to some extent, the behaviour that has been reported by other workers on the passivation of positive plates [21–24]. The similarity is particularly obvious with respect to the role of tin, as a constituent of the grid alloy. A recurring theme in the major studies of positive-plate passivation (PPP) is that tin reduces greatly the high corrosion-layer resistance that develops under certain types of duty [25]. The same effect of tin is apparent in the work discussed here, i.e., under deep-discharge cycling conditions. Apart from the studies of Giess [21], this type of service has seldom been associated with PPP. Indeed, much of the information available to date has suggested that PPP and PCL are largely separate phenomena [25]. By comparison, our work suggests that there may be a much closer relationship between capacity loss and passivation. This new information has been made available

by the measurement of corrosion-layer resistance *in situ*, with grids that have also been subjected, as pasted positive plates, to extensive cycling studies.

Conclusions

The main aim of this work has been to investigate the influence of grid-alloy composition on the incidence of premature capacity loss (PCL) in lead/acid batteries. We have also attempted to clarify the role of several factors with which PCL is associated. The major findings may be summarized as follows:

- antimony in the positive-grid reduces the severity of PCL, but not the incidence of the effect
- increased overcharge, under constant-current charging, enhances the rate of PCL; the effect is greater for Pb–Ca plates than for Pb–Sb analogues
- positive plates with grids that are both antimony-free and tin-free undergo large increases in corrosion-layer resistance during medium- to low-rate discharging

The high resistance observed for Pb–Ca positive plates increases the significance of the distinct bi-layered structure of the corrosion products found in cycled examples of such plates. In addition, the beneficial effect of tin in reducing corrosion-layer resistance now invites a detailed investigation of its effects under cycling duty. At present, this issue is still the subject of keen debate [25].

Acknowledgements

The authors wish to acknowledge the assistance of Dr D.A.J. Rand for useful discussion of the data, Messrs D.G. Vella and A.A. Cargas for construction and maintenance of cell-control equipment, Messrs C.M. MacRae and I.R. Harrowfield for acquisition of electron microprobe data, Ms P.M. Hoobin, C. McInnes and M. Nadal for chemical analyses.

References

1 A.F. Hollenkamp, *J. Power Sources, 36* (1991) 567.
2 S. Tudor, A. Weisstuch and S.H. Davang, *Electrochem. Technol., 3* (1965) 91.
3 S. Tudor, A. Weisstuch and S.H. Davang, *Electrochem. Technol., 4* (1966) 406.
4 S. Tudor, A. Weisstuch and S.H. Davang, *Electrochem. Technol., 5* (1967) 21.
5 H. Nakashima and S. Hattori, *Proc. Pb80 7th Int. Lead Conf., Madrid, Spain, May 12–15, 1980,* p. 88.
6 T.G. Chang, in K.R. Bullock and D. Pavlov (eds.), *Proc. Symp. Advances in Lead-Acid Batteries,* Vol. 84-14, The Electrochemical Society, Pennington, NJ, USA, 1984, pp. 86–97.
7 K. Gibson, K. Peters and F. Wilson, in J. Thompson (ed.), *Power Sources 8,* Academic Press, London, 1981, p. 565.
8 H. Bode, *Lead-Acid Batteries,* Wiley, New York, 1977.
9 A.F. Hollenkamp, K.K. Constanti, A.M. Huey, M.J. Koop and L. Apăteanu, *J. Power Sources, 40* (1992) 125.
10 J.L. Pouchou and F. Pichoir, *Rech. Aerosp., 3* (1984) 167.
11 C.G. Phyland, N.C. Wilson, I.R. Harrowfield, C.M. MacRae and A. Montgomery, *J. Comp. Assist. Microscop., 4* (1992) 271.
12 M. Calábek and K. Micka, in K.R. Bullock and D. Pavlov (eds.), *Proc. Symp. Advances in Lead-Acid Batteries,* Vol. 81-14, The Electrochemical Society, Pennington, NJ, USA, pp. 288–301.

13 M. Calábek and K. Micka, *J. Power Sources, 30* (1990) 315.
14 M. Calábek and K. Micka, *Electrochim. Acta, 37* (1992) 1805.
15 K.K. Constanti, A.F. Hollenkamp, A.M. Huey and D.A.J. Rand, *ILZRO Project LE-371, Progress Rep. No. 1,* CSIRO Division Mineral Products, Melbourne, Australia, Commun. MPC/M-220, Jan. 1991.
16 K.K. Constanti, A.F. Hollenkamp, A.M. Huey and D.A.J. Rand, *ILZRO Project LE-371, Progress Rep. No. 2,* CSIRO Division Mineral Products, Melbourne, Australia, Commun. MPC/M-256, July 1991.
17 K.K. Constanti, J.A. Hamilton, A.F. Hollenkamp, A.M. Huey and L.H. Vu, *ILZRO Project LE-371, Progress Rep. No. 3,* CSIRO Division Mineral Products, Melbourne, Australia, Commun. MPC/M-302, Jan. 1992.
18 W. Borger, U. Hullmeine, H. Laig-Hörstebrock and E. Meissner, in T. Keily and B.W. Baxter (eds.), *Power Sources 12,* International Power Sources Symposium Committee, Leatherhead, Surrey, UK, 1989.
19 A. Winsel, E. Voss and U. Hullmeine, *J. Power Sources, 30* (1990) 209.
20 D. Pavlov, *J. Power Sources, 42* (1993) 345.
21 H.K. Giess, in K.R. Bullock and D. Pavlov (eds.), *Proc. Symp. Advances in Lead-Acid Batteries,* Proc. Vol. 84-14, The Electrochemical Society, Pennington, NJ, USA, 1984, p. 241.
22 K. Wiesener, J. Garche and N. Anastasijevic, in J. Thompson (ed.), *Power Sources 9, Research and Development in Non-mechanical Electrical Power Sources,* Academic Press, 1983, p. 17.
23 H. Döring, J. Garche, H. Dietz and K. Wiesener, *J. Power Sources, 30* (1990) 41.
24 R.T. Barton, P.J. Mitchell and F.A. Fleming, in T. Keily and B.W. Baxter (eds.), *Power Sources 13, Research and Development in Non-mechanical Electrical Power Sources,* International Power Sources Committee, Leatherhead, UK, 1991, p. 25.
25 B. Culpin, A.F. Hollenkamp and D.A.J. Rand, *J. Power Sources, 38* (1992) 63.